The Astrophysical Journal, 981:189 (11pp), 2025 March 10 https://doi.org/10.3847/1538-4357/adab71

An In-depth Study of Gamma Rays from the Starburst Galaxy M82 with VERITAS

A. Acharyya[1], C. B. Adams[2], P. Bangale[3], J. T. Bartkoske[4], W. Benbow[5], J. H. Buckley[6], Y. Chen[7], J. L. Christiansen[8], A. J. Chromey[5], A. Duerr[4], M. Errando[6], M. Escobar Godoy[9], A. Falcone[10], S. Feldman[7], Q. Feng[4], J. Foote[3], L. Fortson[11], A. Furniss[9], W. Hanlon[5], D. Hanna[12], O. Hervet[9], C. E. Hinrichs[5,13], J. Holder[3], T. B. Humensky[14,15], W. Jin[7], M. N. Johnson[9], P. Kaaret[16], M. Kertzman[17], M. Kherlakian[18], D. Kieda[4], T. K. Kleiner[18], N. Korzoun[3], F. Krennrich[19], S. Kumar[14], M. J. Lang[20], M. Lundy[12], G. Maier[18], M. J. Millard[16], C. L. Mooney[3], P. Moriarty[20], R. Mukherjee[21], W. Ning[7], S. O'Brien[12,22], R. A. Ong[7], M. Pohl[18,23], E. Pueschel[24], J. Quinn[25], P. L. Rabinowitz[6], K. Ragan[12], P. T. Reynolds[26], D. Ribeiro[11], E. Roache[5], I. Sadeh[18], L. Saha[5], M. Santander[27], G. H. Sembroski[28], R. Shang[21], M. Splettstoesser[9], D. Tak[29], A. K. Talluri[11], J. V. Tucci[30], V. V. Vassiliev[7], D. A. Williams[9], S. L. Wong[12], J. Woo[31]
(VERITAS Collaboration)
[1] CP3-Origins, University of Southern Denmark, Campusvej 55, 5230 Odense M, Denmark
[2] Physics Department, Columbia University, New York, NY 10027, USA
[3] Department of Physics and Astronomy and the Bartol Research Institute, University of Delaware, Newark, DE 19716, USA
[4] Department of Physics and Astronomy, University of Utah, Salt Lake City, UT 84112, USA
[5] Center for Astrophysics | Harvard & Smithsonian, Cambridge, MA 02138, USA; wbenbow@cfa.harvard.edu, lab.saha@cfa.harvard.edu
[6] Department of Physics, Washington University, St. Louis, MO 63130, USA
[7] Department of Physics and Astronomy, University of California, Los Angeles, CA 90095, USA
[8] Physics Department, California Polytechnic State University, San Luis Obispo, CA 94307, USA
[9] Santa Cruz Institute for Particle Physics and Department of Physics, University of California, Santa Cruz, CA 95064, USA
[10] Department of Astronomy and Astrophysics, 525 Davey Lab, Pennsylvania State University, University Park, PA 16802, USA
[11] School of Physics and Astronomy, University of Minnesota, Minneapolis, MN 55455, USA
[12] Physics Department, McGill University, Montreal, QC H3A 2T8, Canada
[13] Department of Physics and Astronomy, Dartmouth College, 6127 Wilder Laboratory, Hanover, NH 03755, USA
[14] Department of Physics, University of Maryland, College Park, MD, USA
[15] NASA GSFC, Greenbelt, MD 20771, USA
[16] Department of Physics and Astronomy, University of Iowa, Van Allen Hall, Iowa City, IA 52242, USA
[17] Department of Physics and Astronomy, DePauw University, Greencastle, IN 46135-0037, USA
[18] DESY, Platanenallee 6, 15738 Zeuthen, Germany; martin.pohl@uni-potsdam.de
[19] Department of Physics and Astronomy, Iowa State University, Ames, IA 50011, USA
[20] School of Natural Sciences, University of Galway, University Road, Galway, H91 TK33, Ireland
[21] Department of Physics and Astronomy, Barnard College, Columbia University, NY 10027, USA
[22] Arthur B. McDonald Canadian Astroparticle Physics Research Institute, 64 Bader Lane, Queen's University, Kingston, ON K7L 3N6, Canada
[23] Institute of Physics and Astronomy, University of Potsdam, 14476 Potsdam-Golm, Germany
[24] Fakultät für Physik & Astronomie, Ruhr-Universität Bochum, D-44780 Bochum, Germany
[25] School of Physics, University College Dublin, Belfield, Dublin 4, Ireland
[26] Department of Physical Sciences, Munster Technological University, Bishopstown, Cork, T12 P928, Ireland
[27] Department of Physics and Astronomy, University of Alabama, Tuscaloosa, AL 35487, USA
[28] Department of Physics and Astronomy, Purdue University, West Lafayette, IN 47907, USA
[29] SNU Astronomy Research Center, Seoul National University, Seoul 08826, Republic of Korea
[30] Department of Physics, Indiana University Indianapolis, Indianapolis, IN 46202, USA
[31] Columbia Astrophysics Laboratory, Columbia University, New York, NY 10027, USA
Received 2024 October 30; revised 2024 December 31; accepted 2025 January 15; published 2025 March 7

Abstract

Assuming Galactic cosmic rays originate in supernovae and the winds of massive stars, starburst galaxies should produce very-high-energy (VHE; $E > 100$ GeV) gamma-ray emission via the interaction of their copious quantities of cosmic rays with the large reservoirs of dense gas within the galaxies. Such VHE emission was detected by VERITAS from the starburst galaxy M82 in 2008–09. An extensive, multiyear campaign followed these initial observations, yielding a total of 254 hr of good-quality VERITAS data on M82. Leveraging modern analysis techniques and the larger exposure, these VERITAS data show a more statistically significant VHE signal ($\sim$6.5 standard deviations, σ). The corresponding photon spectrum is well fit by a power law ($\Gamma = 2.3 \pm 0.3_{\rm stat} \pm 0.2_{\rm sys}$), and the observed integral flux is F (>450 GeV) $= (3.2 \pm 0.6_{\rm stat} \pm 0.6_{\rm sys}) \times 10^{-13}$ cm^{-2} s^{-1}, or $\sim$0.4% of the Crab Nebula flux above the same energy threshold. The improved VERITAS measurements, when combined with various multiwavelength data, enable modeling of the underlying emission and transport processes. A purely leptonic scenario is found to be a poor representation of the gamma-ray spectral energy distribution (SED). A lepto-hadronic scenario with cosmic rays

following a power-law spectrum in momentum (index $s \simeq 2.25$) and with significant bremsstrahlung below 1 GeV provides a good match to the observed SED. The synchrotron emission from the secondary electrons indicates that efficient nonradiative losses of cosmic-ray electrons may be related to advective escape from the starburst core.

Unified Astronomy Thesaurus concepts: Gamma-ray astronomy (628); Star forming regions (1565); Galactic cosmic rays (567); Star clusters (1567); Gamma-rays (637); Gamma-ray sources (633); High energy astrophysics (739); Non-thermal radiation sources (1119); X-ray sources (1822); Young massive clusters (2049); Space telescopes (1547); Gamma-ray telescopes (634)

1. Introduction

It is believed that Galactic cosmic rays (protons and nuclei) are dominantly accelerated by the winds and supernovae of massive stars (V. L. Ginzburg & S. I. Syrovatskii 1964; H. J. Völk et al. 1996a; Y. Butt 2009, and references therein). Accordingly, galaxies displaying an exceptionally high rate of star formation should harbor a correspondingly high cosmic-ray density. These cosmic rays produce gamma-ray emission via their interaction with interstellar gas and radiation.

M82 is a bright starburst galaxy located in the direction of the Ursa Major constellation at a distance of approximately 12 million lt-yr from Earth. It is an excellent laboratory for understanding the physics of star formation (S. Sakai & B. F. Madore 1999). An active starburst region in its center with a diameter of approximately 1000 lt-yr is home to hundreds of massive stars with a total stellar mass of about 10^4–10^6 $M_\odot$, where $M_\odot$ is the mass of the Sun (H. J. Völk et al. 1996a; V. P. Melo et al. 2005). The galaxy has a star formation rate that is ∼10 times higher than galaxies such as the Milky Way, and its supernova rate is ∼0.1–0.3 yr^{-1}. Most of these supernovae explode near the starburst core, where the gas number density is around 200 cm^{-3} (G. H. Rieke et al. 1980; P. P. Kronberg et al. 1985; A. Weiß et al. 2001; D. M. Fenech et al. 2008). The most recent Type Ia supernova, SN 2014j, within M82 was detected on 2014 January 21 (MJD 56678) by the UCL Observatory (S. J. Fossey et al. 2014; A. Goobar et al. 2014).

Starburst galaxies may be calorimeters for cosmic rays, at least for the electron component (H. J. Voelk 1989), meaning that the particles lose their energy within the system and do not efficiently escape. For example, T. M. Yoast-Hull et al. (2013) calculate steady-state cosmic-ray spectra using a one-zone model assuming a single-value proxy for the varying environmental conditions in the multiphase medium within M82 and find consistency with the calorimeter limit. The VERITAS data on M82 can further test this hypothesis.

Given the high density of cosmic rays and ambient matter, M82 was long viewed as a promising target for detecting high-energy gamma rays. However, it was not detected above 100 MeV by the EGRET experiment (J. J. Blom et al. 1999) or by any early ground-based gamma-ray instrument (T. Nagai 2005; N. Götting 2006). In 2009, the VERITAS collaboration reported the first detection of gamma rays (>700 GeV) from M82 (VERITAS Collaboration et al. 2009). Gamma rays were contemporaneously detected at MeV–GeV energies with the Fermi Large Area Telescope (LAT; A. A. Abdo et al. 2009). These detections, together with the detection of gamma rays from the starburst galaxy NGC 253 by H.E.S.S. (F. Acero et al. 2009) and Fermi-LAT (A. A. Abdo et al. 2009) and the Fermi-LAT detection of star-forming region 30 Doradus in the Large Magellanic Cloud (A. A. Abdo et al. 2010), give strong support to the idea that supernovae and massive-star winds are dominant accelerators of cosmic rays up to energies of $\sim 10^{15}$ eV. Hence, starburst galaxies are considered a prominent, albeit rare, class of GeV–TeV gamma-ray emitter.

The initial detection of M82 is one of the weakest reported by VERITAS; the data yielded only $\sim 4.8\sigma$ post-trials in 137 hr, and the corresponding photon spectral index was not well constrained ($\Gamma = 2.5 \pm 0.6_{\mathrm{stat}} \pm 0.2_{\mathrm{sys}}$). The dedicated long-term observations described here improve the photon spectrum (both in statistics and energy range) and correspondingly reduce the statistical uncertainty on the spectral index.

2. VERITAS Observations and Data Reduction

Very-high-energy (VHE) gamma-ray observations of M82 are performed using the VERITAS array of four 12 m diameter Imaging Atmospheric Cherenkov Telescopes. VERITAS is located at the Fred Lawrence Whipple Observatory in Arizona, USA (31°40′30″ N, 110°57′07″ W, 1268 m above sea level). Each telescope is equipped with a camera of 499 photomultiplier tubes providing a field of view of about $3.^\circ5$. The typical energy threshold of the stereoscopic system is ∼100 GeV, and it provides an energy resolution of ∼15% and angular resolution of $\sim 0.^\circ1$ per event. VERITAS is able to detect a weak source (∼0.6% of the Crab Nebula flux) at 5σ significance in 50 hr of observations at small (<30°) zenith angles (N. Park & VERITAS Collaboration 2015; C. B. Adams et al. 2022).

2.1. Data Analysis

M82 was observed for a total of about 335 hr between 2007 and 2022 at zenith angles between 37° and 50°. The observations were performed in wobble mode (V. P. Fomin et al. 1994) with the source offset by $0.^\circ5$, alternating in each of the four cardinal directions, to enable simultaneous background estimation. After quality cuts, which account for hardware problems and poor atmospheric conditions, 254 hr of high-quality, four-telescope dark time are selected for further analysis. The analysis of these VERITAS data is performed using an up-to-date version of the standard VERITAS Analysis and Reconstruction Software (VEGAS 2.5.9; P. Cogan 2008), following the standard analysis procedure. The data are reduced using the image template method (ITM; J. Christiansen 2017), which provides an improved angular resolution compared to early VERITAS publications. The event-selection criteria for identifying gamma-ray images and removing background cosmic-ray images is optimized for hard-spectrum sources using Crab Nebula data scaled to 1% of their nominal strength. The average energy threshold of this analysis is ∼450 GeV, lower than the prior VERITAS publication on M82 due to an upgrade of the VERITAS cameras completed in 2012 (D. B. Kieda 2011; A. N. Otte et al. 2011).

The VERITAS signal is extracted from a circular region of $\sim 0.^\circ07$ radius centered on the position of M82. The significance of any excess is calculated following Equation (17) of T.-P. Li

Table 1
Results from the Analysis of VERITAS Data on M82

Epoch	T (hr)	On	Off	α	Excess	σ	$F(>450$ GeV) (10^{-13} cm^{-2} s^{-1})	Crab (%)	$F(>700$ GeV) (10^{-13} cm^{-2} s^{-1})
2008–2009	137	220	7106	0.02316	55.4	4.1	$3.4 \pm 1.0_{\rm stat} \pm 0.8_{\rm sys}$	0.4	$1.9 \pm 0.6_{\rm stat} \pm 0.4_{\rm sys}$
2011-2022	117	286	8849	0.02346	79.6	5.2	$3.2 \pm 0.8_{\rm stat} \pm 0.6_{\rm sys}$	0.4	$1.8 \pm 0.5_{\rm stat} \pm 0.4_{\rm sys}$
Total (2008–2022)	254	506	15,955	0.02330	135.0	6.5	$3.2 \pm 0.6_{\rm stat} \pm 0.6_{\rm sys}$	0.4	$1.8 \pm 0.3_{\rm stat} \pm 0.4_{\rm sys}$

Note. The top row (2008–09) is the updated analysis from the epoch originally published in VERITAS Collaboration et al. (2009). The second row is for all data since the original publication. The bottom row is for the entire data set. The quality-selected livetime, the number of gamma-ray-like events in the on- and off-source regions, the normalization for the larger off-source region, the observed excess of gamma rays, and the corresponding statistical significance are shown. The flux is reported above the observation threshold of 450 GeV and is also given in percentage of Crab Nebula flux above the same threshold. For comparison to the flux from the original VERITAS publication, the corresponding flux extrapolated above the higher original threshold of 700 GeV is also given.

& Y.-Q. Ma (1983), where the background is estimated via a ring (inner radius $0.^{\circ}6$ and outer radius $0.^{\circ}8$) centered on the source position (ring background model; D. Berge et al. 2007). As the ring model has an energy-dependent radial acceptance correction, the background is estimated differently for the spectral and flux measurements (reflected region method; D. Berge et al. 2007). There are typically 15–18 nonoverlapping regions, with the same offset ($0.^{\circ}5$) from the center of the VERITAS camera as the source, which are used for the spectral analysis; some potential off-source regions are excluded due to bright stars. The VERITAS results were also independently verified using a second VERITAS analysis software package described in G. Maier & J. Holder (2017).

2.2. Results

A pointlike excess of 135 gamma-ray-like events above the estimated background of 372 events is observed from the direction of M82 in 254 hr of lifetime after the cuts. This excess corresponds to a statistical significance of 6.5 standard deviations (σ), or a chance probability of 4.0×10^{-11}. Table 1 shows the results from the analysis of the VERITAS data for a variety of epochs. While the overall significance is higher, the value observed for the original epoch (4.1σ) is lower than the previous pretrial value (5.0σ). The clear detection from the latter, independent data set clearly confirms the previously reported VHE emission from M82. The time-averaged VHE photon spectrum measured for the entire data set is shown in Figure 1. These data are best fit by a power-law function with a photon index $\Gamma = 2.3 \pm 0.3_{\rm stat} \pm 0.2_{\rm sys}$, with flux normalization $(7.2 \pm 1.2_{\rm stat} \pm 1.4_{\rm sys}) \times 10^{-14}$ cm^{-2} s^{-1} TeV $^{-1}$at 1.4 TeV, in the energy range from 200 GeV to 5 TeV. The χ^2 of the power-law fit is 1.4 for 5 degrees of freedom, corresponding to a probability of 0.92. The observed photon index is in agreement with the early VERITAS result (see $\Gamma = 2.5 \pm 0.6_{\rm stat} \pm 0.2_{\rm sys}$). There is no evidence for a high-energy cutoff in the spectrum, and Section 4 includes a brief discussion on what this implies for the spectrum of the radiating particles.

The observed gamma-ray flux from M82 is $F(>450$ GeV$) = (3.2 \pm 0.6_{\rm stat} \pm 0.6_{\rm sys}) \times 10^{-13}$ cm^{-2} s^{-1}. This corresponds to ~0.4% of the Crab Nebula flux above the same threshold. Extrapolating this flux to the threshold of the original VERITAS publication (VERITAS Collaboration et al. 2009) yields $F(>700$ GeV$) = (1.8 \pm 0.3_{\rm stat} \pm 0.4_{\rm sys}) \times 10^{-13}$ cm^{-2} s^{-1}, which is approximately half of the original value ($F(>700$ GeV$) = (3.7 \pm 0.8_{\rm stat} \pm 0.7_{\rm sys}) \times 10^{-13}$ cm^{-2} s^{-1}). A reanalysis of the original sample (2008–2009 data) with the improved calibration and understanding of the detector and simulations, as well as with the more sensitive ITM analysis technique (J. Christiansen 2018), yields a reduced significance and also a decreased flux ($F(>700$ GeV$) = (1.9 \pm 0.6_{\rm stat} \pm 0.4_{\rm sys}) \times 10^{-13}$ cm^{-2} s^{-1}). While the results remain in reasonable agreement given the large errors on the early measurement, this suggests that the flux difference primarily comes from an improved understanding of the instrument and somewhat from statistical fluctuations in the background, rather than a change in the source over time.

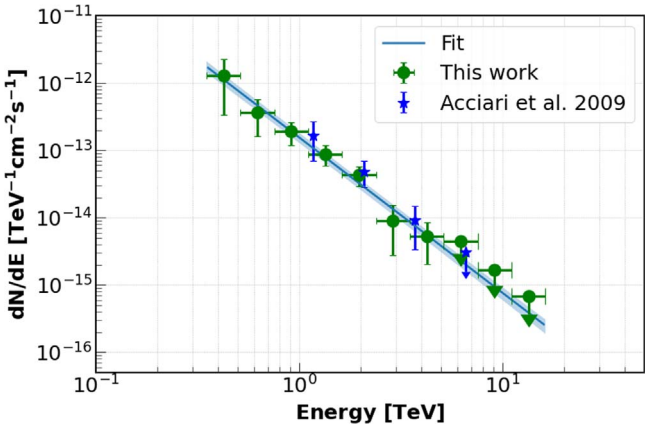

Figure 1. VHE photon spectrum of M82 from the 2008–2022 VERITAS observations. The 2008–2009 result from the previous VERITAS publication (VERITAS Collaboration et al. 2009) is also shown. The 2008–2022 data points are best fit by a power-law function ($\Gamma = 2.3$). The statistical uncertainty for the fit is also shown.

To better illustrate the steady flux observed from M82, the VHE light curve is shown in Figure 2. Here the integral flux above 450 GeV measured for each season (September–July) is plotted. A fit of a constant function to these data ($\chi^2 = 5.4$ for 7 degrees of freedom, $P(\chi^2) = 0.61$), as well as the time-averaged 2008–2022 flux, are also shown. There is no evidence of variability in the seasonal flux measurements.

The best-fit location of the source and its extension are estimated using the methodology discussed in A. U. Abeysekara et al. (2020, and references therein). To estimate the point-spread function (PSF) of VERITAS, Crab Nebula data are analyzed considering VERITAS data from similar epochs and zenith angle coverage to M82. Although a slight extension (~$1'$) of the Crab Nebula was discovered at GeV–TeV energies (H. E. S. S. Collaboration 2020; F. Aharonian et al. 2024), this small effect is not accounted for in this analysis. The PSF is modeled using a 2D Moffat function, as described by the

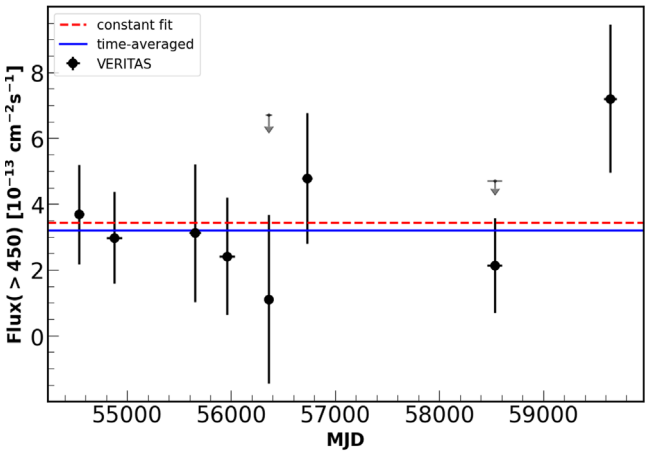

Figure 2. The integral flux above 450 GeV observed by VERITAS during each season. Upper limits (99% confidence level) are also shown for the 2012–2013 and 2018–2019 seasons due to the low significance observed. The time-averaged flux measured during the entire observation period (2007–2022) is indicated by a solid blue line. A fit of a constant to the seasonal data is shown by the dashed red line.

following equation:

$$K(x, y) = A\left[1 + \frac{(x - x_0)^2 + (y - y_0)^2}{\gamma^2}\right]^{-\alpha}. \quad (1)$$

Here, x_0 and y_0 denote the positions of the maximum of the Moffat model in the x- and y-directions, respectively. γ and α represent the core width and power index of the Moffat model. The values of α and γ are estimated to be 2.41 and 0.069, respectively. The best fit for the location (J2000) of the peak of the VERITAS gamma-ray emission is given by R.A. $=9^h55^m48.^s6 \pm 5.^s5_{\rm stat} \pm 4.^s8_{\rm sys}$ and decl. $=+69°39'58.''5 \pm 28.''8_{\rm stat} \pm 25''_{\rm sys}$. It is consistent with the position of M82 as given in N. Jackson et al. (2007; i.e., within an angular separation of $0.^\circ014$) and is named VER J0955 +696. It is also evident from the sky map of the region surrounding M82 (see Figure 3) with the PSF at the bottom left corner that the VERITAS excess is pointlike at GeV–TeV energies. The upper limit on the extension of the VHE excess from M82 is determined to be $1.'9$ at a 95% confidence level.

The best-fit location of the emission observed by VERITAS from M82 and the core position of the Galaxy are shown in Figure 3. This best-fit location is $\simeq 0.9\sigma$ away from the core position of M82 when both the systematic and statistical errors are considered, suggesting that these two locations are consistent with each other. Significantly more data would be needed to try to distinguish whether the origin of the gamma-ray emission differs from the core of the galaxy based on positional information alone.

3. Multiwavelength Data

In addition to VERITAS data, archival fluxes observed in different wave bands, from radio through high-energy gamma rays, are considered for the modeling of M82. Only spectral data points resulting from the nonthermal emission processes are considered. Brief details of these observations are discussed below.

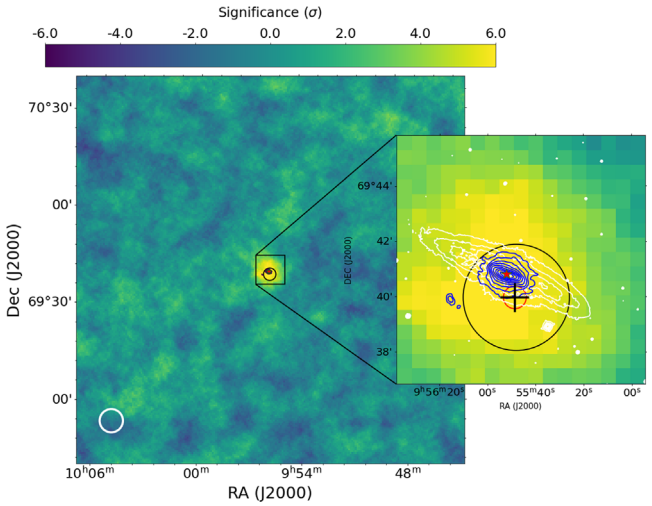

Figure 3. Sky map of significance observed by VERITAS from the region near M82. The position of M82 is indicated with a red star (N. Jackson et al. 2007). The total power radio continuum contours (blue) at about 10 GHz from the WSRT observations are overlaid on the sky map (see Figure 3 of B. Adebahr et al. 2013). These radio contours start at the 3σ level of 50 μJy beam^{-1}, with a beam size of $7.''8 \times 7.''3$, and increases in powers of 2. The data for optical contours (white) at the g band are taken from the survey data of stellar structure in galaxies by Spitzer (J. H. Knapen et al. 2014). The optical contour starts at 16 mag and goes to 1 in steps of 2.143. The black circle indicates the upper limit of the extension ($1.'9$) of M82 as discussed in Section 2. The best-fit location with 1σ statistical errors is shown with a black cross. The 1σ systematic uncertainties are shown around the best-fit centroid position with a red circle. The white circle indicates the VERITAS PSF (68% containment radius) at the average energy threshold of ~450 GeV.

3.1. Radio Observations

The first radio observation of M82 was conducted more than 30 yr ago by J. J. Condon (1992). Later, M82 was imaged at 327 MHz with $40''$ resolution using the Westerbork Synthesis Radio Telescope (WSRT) by B. Adebahr et al. (2013). These observations established that M82 has a radio-bright extended halo structure. Figure 4 displays the radio spectrum above 0.8 GHz (U. Klein et al. 1988; J. E. Carlstrom & P. P. Kronberg 1991; P. K. G. Williams & G. C. Bower 2010; A. Basu et al. 2012; B. Adebahr et al. 2013). At frequencies below ~1 GHz, free–free absorption is expected to modify the spectrum (M. Pohl 1994), and data in this frequency band are not considered.

3.2. X-Ray Observations

M82 is extensively studied in the X-ray band. Using data from Chandra and NuSTAR shows that M82 hosts two ultraluminous X-ray sources: X-1, an intermediate-mass black hole candidate, and X-2, an ultraluminous X-ray pulsar (H. Matsumoto et al. 2001; M. Bachetti et al. 2014). While Chandra observations provide high spatial resolution in the 0.5–8 keV band, NuSTAR provides sensitive spectral coverage above 10 keV. M. Brightman et al. (2020) studied the spectral evolution of X-1 and X-2, finding that the total X-ray emission from M82 is highly variable, most likely due to X-1. For the multi-wave-band spectral modeling, only the diffuse emission components in the energy range above ~1.25–8 keV are considered, and the flux attributable to the compact sources is subtracted. Since the diffuse emission could still be a mix of other compact sources, thermal emission, and a nonthermal

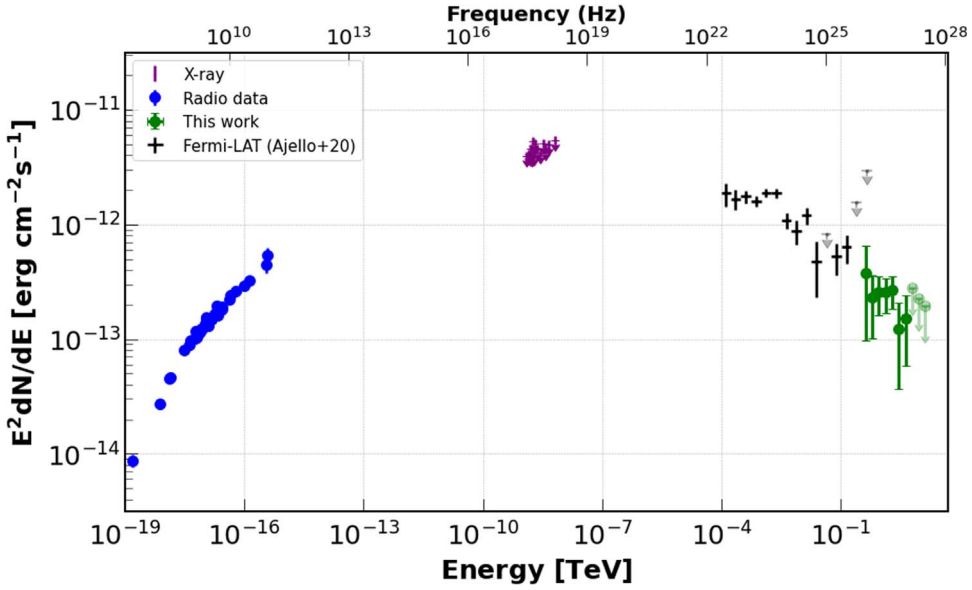

Figure 4. The SED of M82 from radio to TeV energies. The radio data are compiled from observations discussed in Section 3.1 and are shown with a single marker (circle) and color (blue). The X-ray data in the energy range of 1.25–6.5 keV are shown by lines (purple) and taken from M. Brightman et al. (2020). The Fermi-LAT data are taken from M. Ajello et al. (2020). The VERITAS data are the results presented in this paper.

component, the diffuse flux component is treated as an upper limit for constraining the emission models.

3.3. MeV–GeV Gamma-Ray Observations

Using roughly 10 yr of gamma-ray data taken by Fermi-LAT (M. Ajello et al. 2020), M82 is studied in the energy range $E = [0.1, 800]$ GeV. The starburst galaxy is detected with a significance of 34.4σ, corresponding to an integral flux above 1 GeV of $(1.13 \pm 0.05) \times 10^{-11}\,\mathrm{cm^{-2}\,s^{-1}}$. The photon spectrum is best fit by a power law with index $\Gamma = 2.14 \pm 0.06$, which is consistent with the spectral shape in the VHE band. No variability is observed in the 10 yr of Fermi-LAT observations from M82.

4. Modeling the SED

The observed emission can be interpreted with leptonic and hadronic emission models. Early assessments, prior to the gamma-ray detection of M82, predicted a GeV-scale flux a factor of a few below the sensitivity limit of EGRET (M. Pohl 1994; M. Persic et al. 2008). An important finding was that the radio synchrotron emission from secondary electrons produced in the same interactions that create hadronic gamma rays should be particularly bright, on account of the rapid energy losses of electrons and the typical duration of starburst events. Therefore, the hadronic gamma-ray output could not be arbitrarily bright, and it would always be accompanied by leptonic radiation in the radio and X-ray bands.

4.1. Leptonic Scenario

Within a purely leptonic scenario, the emission from electrons has to account for the entire nonthermal SED, in particular the bright GeV-scale emission with flux $\nu F_\nu \approx 10^{-12}\,\mathrm{erg\,cm^{-2}\,s^{-1}}$. There are two relevant radiation processes in this energy band, nonthermal bremsstrahlung and inverse-Compton scattering (G. R. Blumenthal & R. J. Gould 1970).

Table 2
Fiducial Parameter Values for Our Radiation Modeling

Parameter	Value	Unit
n_{H}	200	$\mathrm{cm^{-3}}$
n_e	50	$\mathrm{cm^{-3}}$
U_{mag}	500	$\mathrm{eV\,cm^{-3}}$
U_{rad}	500	$\mathrm{eV\,cm^{-3}}$

Note. From top to bottom, we list the density of neutral (see P. A. Smith et al. 1991; A. Weiß et al. 2001; B. J. Naylor et al. 2010) and ionized gas, and also the energy density of the magnetic field, here estimated above cosmic-ray equipartition on account of turbulent amplification (A. A. Schekochihin & S. C. Cowley 2007; J. Cho et al. 2009), and the ambient infrared radiation (D. H. Hughes et al. 1994; N. M. Förster Schreiber et al. 2003).

The interstellar medium (ISM) in M82 is composed of very dense molecular clouds; dense, warm, ionized gas; and a hot, low-density medium in approximate pressure balance (M. S. Westmoquette et al. 2009). One can simplify the complex structure as a uniform zone with "mean" values for the environmental parameters, as was done in other studies (e.g., M. Pohl 1994; M. Persic et al. 2008; E. de Cea del Pozo et al. 2009; B. C. Lacki & T. A. Thompson 2012; T. A. D. Paglione & R. D. Abrahams 2012; T. M. Yoast-Hull et al. 2013). Among these studies, there is a range of "mean" parameter values that were adopted. The fiducial values used here are in the middle of this range and are listed in Table 2. To reflect the impact of the uncertainty in the parameters, one can add scaling factors to the equations where applicable. In any case, the ratios of the parameter values display considerably less variation than do the values themselves, which renders estimates of the energy partition between the various radiation and energy-loss channels reasonably well defined.

Relativistic electrons are known to quickly lose energy through various channels on a timescale that is shorter than the duration of the starburst in M82 (N. M. Förster Schreiber et al. 2003). The total energy-loss rate, $b(E)$, can be written as

(M. Pohl 1993)

$$-b(E) = C_1 + C_2\,E + C_3\,E^2, \tag{2}$$

where

$$C_1 = (3.7 \cdot 10^{-16} \quad \mathrm{GeV\ s^{-1}})\,(n_\mathrm{H} + 1.54\,n_e),$$
$$C_2 = (10^{-15} \quad \mathrm{s^{-1}})\,(n_\mathrm{H} + 0.95\,n_e),$$
$$C_3 = (10^{-16} \quad \mathrm{GeV^{-1}\,s^{-1}})\,(U_\mathrm{mag} + U_\mathrm{rad}).$$

This includes the loss rates for ionization and Coulomb scattering (C_1), nonthermal bremsstrahlung (C_2), and synchrotron emission and inverse-Compton radiation (C_3). The energy densities of the magnetic field and the soft radiation, U_mag and U_rad, are in units of eV cm^{-3}, and the number densities of atomic (n_H) and ionized (n_e) gas are in cgs units. For simplicity, inverse-Compton scattering in the Thomson limit is assumed; this should be well justified for the production of GeV-scale gamma rays.

If the rate of cosmic-ray production during the starburst phase in M82 was high for more than a few hundred thousand years, then the system would be calorimetric for electrons at energies around 1 GeV and higher (H. J. Voelk 1989). In this calorimetric limit, a spectral break in the energy-loss rate imposes a corresponding feature in the electron spectrum,

$$N(E) = \frac{1}{|b(E)|}\int_E dE' Q(E'), \tag{3}$$

where $Q(E)$ is the source spectrum of electrons. A first change in the energy dependence of the loss rate, $E/|b(E)|$, is observed at about $E_{c1} = C_1/C_2 \simeq 0.4$ GeV, which for $U_\mathrm{mag} \approx 500$ would appear at the same photon energy ($1.5 \cdot 10^{-18}$ TeV or 400 MHz) at which free–free absorption may become significant (M. Pohl 1994). One can ignore synchrotron photon energies below 1 GHz and therefore neglect the term C_1 in the loss rate.

A second spectral feature should appear at

$$E_{c2} = \frac{C_2}{C_3} \simeq (2.5\ \mathrm{GeV})\frac{1000(n_\mathrm{H} + 0.95\,n_e)}{245(U_\mathrm{mag} + U_\mathrm{rad})}, \tag{4}$$

where the number and energy densities are in cm^{-3} and eV cm^{-3}, respectively, and the numerical factors derive from the fiducial values of the parameters (see Table 2). The spectral break should be seen in the radio spectrum at the frequency

$$\nu_{c2} \simeq (15\ \mathrm{GHz})\sqrt{\frac{U_\mathrm{mag}}{500}}\left(\frac{1000(n_\mathrm{H} + 0.95\,n_e)}{245(U_\mathrm{mag} + U_\mathrm{rad})}\right)^2. \tag{5}$$

The frequency 15 GHz corresponds to a photon energy of $6 \cdot 10^{-17}$ TeV. No evidence of a high-frequency break in the radio synchrotron spectrum is seen, although it should be there, because the lifetime of the radiating electrons ($<10^5$ yr) is very much shorter than the starburst duration and the evolutionary timescale of massive stars.

The absence of a visible spectral break suggests that the scaling factor might be larger than unity. However, the flux points above 20 GHz (10^{-16} TeV) could include dust emission or thermal bremsstrahlung, in which case the scaling factor for the energy-loss break could be close to unity. The spectral break near $E_\gamma \approx 10^{-18}$ TeV (200 MHz) in the radio spectrum may reflect free–free absorption. Indeed, homogeneously distributed ionized gas at 3000 K temperature that subtends a solid angle of $\Delta\Omega \approx 3 \cdot 10^{-8}$ sr and provides an opacity of unity at 400 MHz would provide a flux at 100 GHz of (K. Rohlfs & T. L. Wilson 2004, Section 9.4)

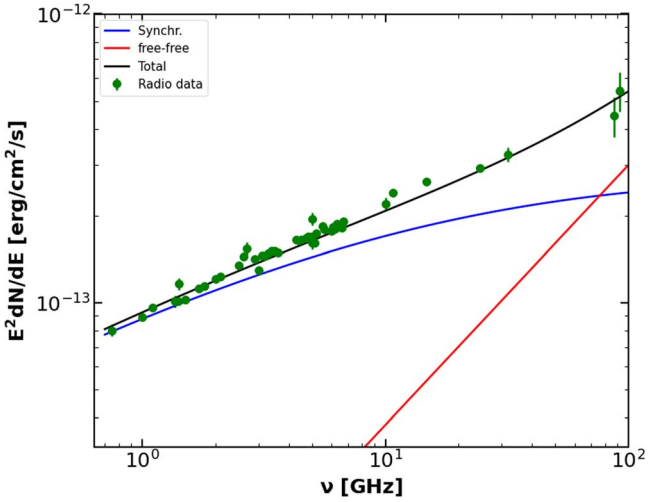

Figure 5. Radio SED of M82 compared with a model spectrum that is composed of a synchrotron component following Equation (3) with $Q \propto E^{-2.25}$ and free–free emission with a flux slightly below the estimate in Equation (6). The radio data are taken from U. Klein et al. (1988), J. E. Carlstrom & P. P. Kronberg (1991), P. K. G. Williams & G. C. Bower (2010), A. Basu et al. (2012), and B. Adebahr et al. (2013).

$$E^2\frac{dN}{dE}_{\mathrm{free-free}}(100\ \mathrm{GHz}) \approx 3 \cdot 10^{-13}\mathrm{erg/cm^2\,s^{-1}}, \tag{6}$$

which is nearly the entire observed flux. It is therefore likely that in the band 10–100 GHz, the transition from synchrotron-dominated emission to thermal radiation is seen.

Figure 5 displays the radio spectrum in comparison with a free–free emission component and a synchrotron component for a scaling factor of unity (see Equation (5)) and a spectrum according to Equation (3) with $Q \propto E^{-2.25}$. The reasonable match between the model and data is notable, although the parameters have only been coarsely optimized.

There will be a bremsstrahlung contribution to the GeV-scale gamma-ray emission, and, using the differential cross section for bremsstrahlung given in G. R. Blumenthal & R. J. Gould (1970) and our fiducial parameters, the observed radio synchrotron spectrum in the frequency band 1–10 GHz can be turned into an estimate for the bremsstrahlung spectrum that is displayed in Figure 6. More specifically, the fraction of the observed flux at $E = 0.15$ GeV provided by bremsstrahlung is

$$\frac{F_\mathrm{bre}(0.15\ \mathrm{GeV})}{F_\mathrm{obs}(0.15\ \mathrm{GeV})} \simeq 0.8\,\frac{n_\mathrm{H} + 0.95n_e}{245}\left(\frac{500}{U_\mathrm{mag}}\right)^{5/6}, \tag{7}$$

where, as in Equation (4), the number and energy densities are in cm^{-3} and eV cm^{-3}, respectively, and the numerical factors derive from the fiducial values of the parameters. This fraction of flux rapidly falls off with energy, and for the fiducial parameter values corresponds to only 30% at 1 GeV. To be noted from Equation (7) is that the parameter scaling factor for the bremsstrahlung flux cannot be much larger than unity, otherwise the bremsstrahlung flux would overshoot the observed gamma-ray flux near 0.1 GeV.

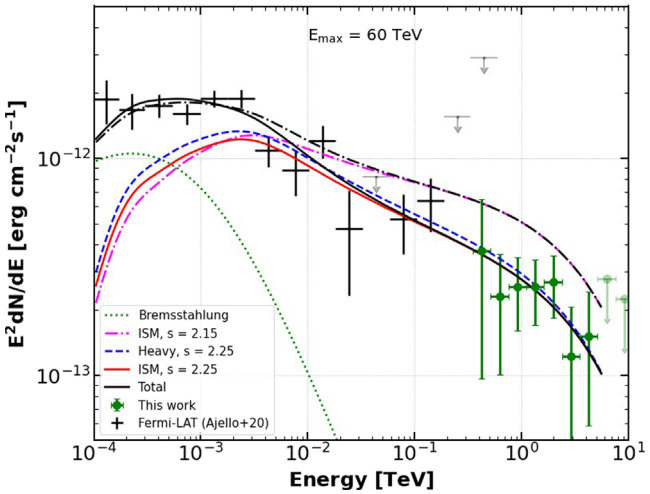

Figure 6. Gamma-ray SED of M82 compared with hadronic models, varying the spectral index and the elemental composition. The bremsstrahlung contribution is given by the green dotted line. The maximum particle energy, $E_{\rm max}$, is set to 60 TeV. The black solid line is the sum of bremsstrahlung and the hadronic component for ISM and $s = 2.25$; likewise, the black dashed–dotted line is for $s = 2.15$.

If the observed gamma-ray emission near 10 GeV were the result of inverse-Compton scattering of the far-infrared (FIR) radiation field (N. M. Förster Schreiber et al. 2003), then the radiating electrons would have an energy of about 500 GeV. This is high enough for the electrons to be efficiently cooled, and the spectral index should be softer by half than that of the radio synchrotron emission, implying a spectral index $\alpha = -2.13$ in dN/dE. The observed gamma-ray spectrum has a similar shape up to about 1 TeV, where the maximum electron energy and the Klein–Nishina transition would introduce a decline of flux.

The synchrotron radiation from these 500 GeV electrons would be observed in the optical, at 1 eV or 10^{-12} TeV, where starlight dominates. As Thomson scattering off the FIR photons applies and the energy-loss rates for synchrotron and inverse-Compton emission are similar, so are the νF_ν flux and the spectral index at corresponding energies, 10 GeV for inverse-Compton emission and 10^{-12} TeV for the synchrotron radiation. The Klein–Nishina transition is expected to be slightly higher in gamma-ray energy, near 1 TeV. Extrapolating the synchrotron spectrum to 10^{-12} TeV (see Figure 5) and using the fiducial ratio $U_{\rm rad}/U_{\rm mag} = 1$, we estimate that inverse-Compton scattering only provides about 10% of the flux at 10 GeV.

A significant contribution to the GeV-to-TeV gamma-ray emission from M82 would require the ratio $U_{\rm rad}/U_{\rm mag}$ to be much larger than unity. The FIR intensity distribution is well measured, and hence $U_{\rm rad}$ is well determined, but there is uncertainty in the energy density of the magnetic field. If it were smaller than 500 eV cm^{-3} by a certain factor, then the gas density in the starburst core would need to be reduced in a similar way, otherwise the bremsstrahlung flux at a few hundred MeV would overshoot the observed flux (see Equation (7)). Indeed, the bremsstrahlung flux needs to significantly undershoot the observed flux, because unlike for the hadronic emission scenario, the inverse-Compton component provides approximately the same fraction of the 100 MeV flux as it does to the 10 GeV flux. The modifications of the gas density and the magnetic field strength drive the break frequency in the radio spectrum (Equation (5)) well below 1 GHz. This would need to be compensated for with a harder production spectrum of electrons, otherwise the observed radio spectrum would be poorly reproduced. Reducing the energy density of the magnetic field by a factor of 3, and likewise the gas density, already requires a source spectrum $Q \propto E^{-1.9}$, and the inverse-Compton spectrum would no longer match the observed gamma-ray spectrum.

We conclude that a purely leptonic scenario for the SED of M82 is very unlikely, although bremsstrahlung may provide a significant contribution to the observed gamma-ray flux below 1 GeV. If that is the case, the electron-to-ion ratio of cosmic rays in M82 would be unusually large with 10% or more at a few GeV.

4.2. Hadronic Scenario

The winds of massive stars in the starburst region, as well as the resulting supernova explosions, will enrich the gas with metals that likely lead to a heavy composition of the cosmic-ray hadrons. By analyzing the gamma-ray SED, the spectrum of cosmic-ray nuclei and their composition can potentially be extracted, assuming they account for most of the measured GeV/TeV flux.

Here, η_A is denoted as the fraction in number of a certain element with mass number A. It is simple to apply this factor to the target material, but it must also be accounted for in the cosmic-ray spectra. For calculation of the gamma-ray spectra, a model derived with the Monte Carlo event generator DPMJET III is used; this model is described in M. Bhatt et al. (2020). The emissivities are binned for cosmic-ray spectra written in total energy per nucleon, E_A. The actual particle acceleration scales with momentum per charge, known as the rigidity, $r = p/Z$. All cosmic rays are most likely injected at the same rigidity, because of a requirement that particles can cross the shock without significant deflection, and their spectrum terminates at the same maximum rigidity.

The energy per nucleon and the rigidity are related as

$$E_A = \sqrt{m^2c^4 + \frac{Z^2}{A^2}r^2c^2}\,, \tag{8}$$

where m denotes the proton rest mass and c is the speed of light. It follows that the maximum particle energy scales as

$$E_{A,\rm max} \propto \frac{Z}{A}. \tag{9}$$

The injection rigidity of all particles being the same, the injection energy varies with mass and charge number, following Equation (8). The modeling ignores that heavy elements may initially be locked up in dust particles (e.g., D. C. Ellison et al. 1997; J.-P. Meyer et al. 1997). For a power-law spectrum in rigidity with index s and step functions for the smallest ($r_{\rm inj}$) and the largest rigidity ($r_{\rm max}$),

$$N(r) = N_0 r^{-s}\,\Theta(r - r_{\rm inj})\,\Theta(r_{\rm max} - r), \tag{10}$$

the corresponding spectrum in total energy per nucleon is

$$N(E_A) = \eta_A\, N_0\, E_A \left(\frac{A}{Z}\right)^{1-s} (E_A^2 - m^2c^4)^{-(1+s)/2} \times \Theta(E_A - E_{A,\rm inj})\,\Theta(E_{A,\rm max} - E_A). \tag{11}$$

Table 3
Number Fractions of the Elements Considered in the Two Models of Composition

Components	ISM	Heavy
Hydrogen	0.909	0.848
Helium	0.090	0.146
Carbon	2.1e-4	5.2e-3
Oxygen	1.6e-4	7.e-4

Note. Following A. Sander et al. (2012), H. Todt et al. (2015), L. Dessart et al. (2017), and A. A. C. Sander et al. (2019).

The overall normalization, N_0, should be the same for all elements, because the abundances are accounted for with the factor η_A.

This model is considered with the elements hydrogen, helium, carbon, and oxygen matching the ISM composition and, as a test case, with the number fractions matching 40% ISM, 40% red supergiant winds, and 10% each WN and WC Wolf–Rayet stars. The composition fractions are listed in Table 3 and are applied to both the cosmic rays and the target gas. All cosmic rays are assumed to be fully ionized.

Figure 6 displays the gamma-ray SED in comparison with three model spectra and the bremsstrahlung component derived in Section 4.1. The normalization of the models has been determined by eye adjustment only on account of the systematic uncertainties in the bremsstrahlung contribution and emission from outside of the starburst core. To be noted from the figure are three points.

1. Whereas the spectrum above a few GeV appears to be well represented by a power law, the maximum proton energy, $E_{\rm max}$, is poorly constrained and may be below 60 TeV.
2. A heavy composition provides additional gamma-ray flux below a few GeV, but the uncertainties of the spectral data and the bremsstrahlung contribution are too large for conclusions on the composition.
3. With the bremsstrahlung component as derived with the fiducial values for the gas density and the magnetic field strength, a power-law spectrum in rigidity with index $s = 2.25$ provides a reasonable match between the model and the entire gamma-ray SED. A spectral index $s = 2.15$ is already at the limit of acceptability, because it overshoots the observed flux above a few hundred GeV, although the hardness of the spectrum can, within limits, be compensated for by choosing a lower maximum energy.

In the absence of a leptonic contribution, the power-law index of the cosmic-ray nuclei should be $s = 2.35$, and the first data point at 130 MeV cannot be reproduced.

4.3. Secondary Electrons

An unavoidable side product in the hadronic scenario is a copious supply of secondary electrons (subsuming electrons and positrons) that result from the production and decay of charged pions. The source rate of electrons is approximately the same as that of gamma rays, but their energy is slightly lower. Then, GeV-scale gamma-ray emission implies electron production at a Lorentz factor $\gamma_e \approx 10^3$. For an elevated production of secondary electrons lasting 10^6 yr or more, M82 would be in the calorimetric limit (H. J. Voelk 1989), and the radio flux produced by secondary electrons would reach a constant value. The bolometric nonthermal luminosity would be a direct measure of the cosmic-ray production power. Again using the fiducial parameters (see Table 2), the energy-loss timescale of cosmic-ray nuclei is estimated to be $\tau_{\rm loss\ pp} \simeq 3 \cdot 10^5$ yr over the energy range between 10 GeV and 10 TeV (C. Y. Huang et al. 2007). Although the starburst activity in M82 is not constant (I. S. Konstantopoulos et al. 2009), the recent spike probably happened about 10 million yr ago, with strong stellar winds and an elevated supernova rate since then. This is significantly longer than the time needed to reach calorimetry for hadronic and leptonic cosmic rays. Hence, the distribution of secondary electrons should be in the steady state.

The synchrotron flux from the secondary electrons with $E \approx 1$ GeV, or $\gamma_e \simeq 2 \cdot 10^3$, that is observable at about 3 GHz in frequency, or $E_\gamma \approx 10^{-17}$ TeV, would have to be a factor of approximately 15 weaker than the νF_ν flux of the pion-decay gamma rays at 1–2 GeV. This factor of 15 is the product of a factor of 5 for the fraction of energy loss; a factor of 2 for the synchrotron Jacobian, dE/dE_γ; and a factor of 1.5 for the efficiency ratio of gamma rays and electrons. The observed flux is about at this expected value, indicating that a large fraction of the GeV-scale electrons in M82 may be secondary. The following investigates this in more detail to infer whether additional loss processes could be at play.

To explore the contribution of secondary electrons to the radio spectrum at all frequencies, their production rate, Q_e, is calculated with the same model (M. Bhatt et al. 2020) used in Section 4.2 to determine the emissivity of hadronic gamma rays (see also C. Y. Huang & M. Pohl 2008). For simplicity, only a spectral index $s = 2.25$ and ISM composition is considered, corresponding to the dark red curve in Figure 6. The steady-state electron spectrum, $N = dN/dE$, is well described by the continuity equation:

$$\frac{\partial}{\partial E}(b(E)\,N) + \frac{N}{T} = Q_e(E). \tag{12}$$

Here T is the timescale of catastrophic losses that remove particles, for example, escape in the wind. For simplicity, it is assumed to be independent of energy. The solution to Equation (12) is well known (N. S. Kardashev 1962),

$$N(E,\,t) = \int_E^\infty dE' \quad \frac{Q_e(E')}{|b(E)|}\ \exp\left(-\int_E^{E'} \frac{du}{T\ |b(u)|}\right), \tag{13}$$

where $b(E)$ is the energy-loss rate (Equation (2)).

The omnidirectional synchrotron emissivity of a single electron can be written in monochromatic approximation as

$$P_{E_\gamma} = \frac{E^2}{(10^{16}\quad \text{GeV s})}\, U_{\rm mag}\ \delta(E_\gamma - aE^2), \tag{14}$$

where

$$a = (4 \cdot 10^{-16}\quad \text{GeV}^{-1})\ \sqrt{U_{\rm mag}}. \tag{15}$$

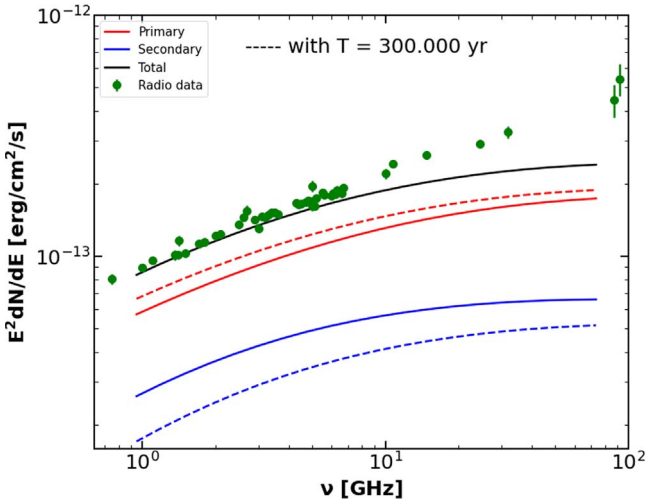

Figure 7. Radio SED of M82 compared with synchrotron emission spectra from secondary electrons and positrons for the baseline hadronic models (blue lines) with spectral index $s = 2.25$ and ISM composition. The solid black line indicates the total synchrotron flux (the same as the blue line in Figure 5), and the red lines reflect the contribution of primary electrons. Dashed lines show spectra calculated accounting for catastrophic losses with timescale $T = 3 \cdot 10^5$ yr.

The emission coefficient, j_{E_γ}, for synchrotron radiation then is calculated as

$$E_\gamma j_{E_\gamma} = E_\gamma \int dE \quad P_{E_\gamma} N(E, t) = \frac{1}{1 + \frac{U_{\rm rad}}{U_{\rm mag}}} \frac{E_1^2}{2\left[E_1 + E_{c2}\left(1 + \frac{E_{c1}}{E_1}\right)\right]} \boldsymbol{I}, \tag{16}$$

where

$$\boldsymbol{I} = \int_{E_1}^{\infty} dE' \quad Q_e(E') \exp\left(-\int_{E_1}^{E'} \frac{du}{T\ |b(u)|}\right) \tag{17}$$

and

$$E_1 = \sqrt{\frac{E_\gamma}{a}}. \tag{18}$$

Figure 7 compares radio flux measurements from the literature with the expected synchrotron spectra of secondary electrons and positrons alone (Equation 16). The source rate of secondary electrons, Q_e in Equation (12), corresponds to the gamma-ray emission model with cosmic-ray spectral index $s = 2.25$ and ISM composition that in Figure 6 was shown to match the observed GeV/TeV spectrum very well.

The synchrotron flux from secondary electrons in the calorimetric limit is about one-third of the observed flux at a few GHz, approximately scaling with the inverse of the scaling factor for the bremsstrahlung flux (see Equation (7)). As previously noted in Section 4.2, this factor cannot significantly exceed unity, and in consequence, the scaling factor for the radio flux from secondary electrons may not significantly fall below unity.

This leaves two-thirds or less of the radio flux to be provided by primary electrons. There is little spectral difference between the synchrotron emission from primary and secondary electrons, largely because their source spectra are found to be similar above 1 GeV. The inhomogeneity in the starburst core makes estimating a mean magnetic field and mean gas density difficult, and it may be that the magnetic field is substantially weaker than the fiducial value or the gas density much higher than that given in Table 2, reducing the synchrotron emission from secondary electrons. However, this would imply more GeV-scale electrons in the system and hence a larger bremsstrahlung flux that would exceed the observed gamma-ray flux at 100–500 MeV.

An alternative option is another loss process on a similar timescale that is not accounted for here. Figure 7 also contains the expected radio spectrum from secondary electrons in the calorimetric limit with an additional catastrophic loss on the timescale $T = 3 \cdot 10^5$ yr, for which the contribution of primary electrons to the GHz-scale synchrotron flux could rise to about 75%. Such a loss process may be advection in the starburst wind, in which localized driving and radiative cooling lead to a multiphase structure composed of filaments of dense gas embedded in a very dilute gas that flow at high speed (e.g., C. Melioli et al. 2013). Advective transport out of the starburst core over a distance of 300 pc in a wind moving at 1000 km s^{-1} would take $\tau_{\rm adv} \simeq 3 \cdot 10^5$ yr, sufficient to significantly reduce the radio emission from secondary electrons.

4.4. The Cosmic-Ray Spectrum

If limited by available time and not by any loss process, the spectrum of cosmic rays should reflect the spectrum with which the particles are produced. Otherwise, the losses may modify the spectrum. Again using the aforementioned fiducial parameters (see Table 2), the energy-loss timescale of cosmic-ray nuclei is estimated to be $\tau_{\rm loss\ pp} \simeq 3 \cdot 10^5$ yr with little variation over the energy range between 10 GeV and 10 TeV (C. Y. Huang et al. 2007). For cosmic-ray electrons, $\tau_{\rm loss\ e} \simeq 10^5$ yr at 1 GeV, corresponding to synchrotron radiation at a few GHz, with a transition to a decreasing lifetime above that energy. In the previous section, it was shown that additional loss processes, possibly advective escape, may be at play with a lifetime similar to that of the energy losses.

A complication for advective escape lies in the diffusive transport between the dense filaments, where most of the radiation is produced, and the dilute, fast-flowing gas that provides advective transport. To our knowledge, there is no assessment of cosmic-ray spectra in a complex environment like that in M82. There are analytical 1D estimates of cosmic-ray transport in an accelerating wind that suggest that even in the steady state for losses by advection, the cosmic-ray spectrum would be the production spectrum steepened by half of the energy dependence of the diffusion coefficient (I. Lerche & R. Schlickeiser 1982), and so the observed spectral index must be close to the mean production spectral index. For cosmic-ray ions in M82, we found a spectral index $s = 2.25$. The radio spectrum, for comparison, is compatible with a source spectral index $s \simeq 2.25$ for electrons in the energy range 1–10 GeV.

The production spectral index around $s \simeq 2.25$ deduced for the cosmic rays in M82 is somewhat softer than that provided by diffusive shock acceleration. Simulations suggesting a spectral softening on account of different downstream advection speeds of gas and magnetic turbulence have been reported (D. Caprioli et al. 2020) but have not been independently confirmed to date. Energy loss by driving of turbulence has been shown to have very little, if any, effect on the spectrum (M. Pohl 2021).

The particle spectrum produced at a certain time and the time integral of the production spectrum are two different quantities. Relevant for the analysis offered in this paper is the latter, and diffusive shock acceleration provides the former. Studies of supernova remnants indicate that with time, the interplay of turbulence driving in the upstream region and particle acceleration at the shock becomes less efficient, primarily resulting in a reduction of the maximum particle energy that can be reached (S. Celli et al. 2019; R. Brose et al. 2020). The time integral of the production spectrum would be slightly softer than what we deduced for M82 above a few GeV, with an effective spectral index of $s \approx 2.4$.

The supernova remnants and the wind bubbles of massive stars in M82 are likely overlapping, leading to a complex and turbulent structure composed of hot, dilute plasma and cool, dense gas organized in shells (D. V. Badmaev et al. 2022). The situation resembles a supernova remnant in the wind bubble of a Wolf–Rayet progenitor (e.g., D. M. A. Meyer et al. 2020) and interacting supernova remnants like IC 443 (S. Ustamujic et al. 2021). If a supernova shock passes through plasma that has been shocked before by another supernova or a wind termination shock, then the temperature is very high and the sonic Mach number low, resulting in a soft particle spectrum with low cosmic-ray density (e.g., S. Das et al. 2022). If the supernova shock hits a filament of dense gas or the outer shell of a collective wind bubble, it splits into a reflected shock that provides little acceleration to high energies, as well as a transmitted shock that will propagate through the dense gas. Many particles may be accelerated by the transmitted shock, but its speed is low, and so is the maximum energy to which it can accelerate.

5. Summary

The VERITAS collaboration performed a long-term study of the starburst galaxy M82 at GeV–TeV energies using more than 10 yr of data. This study primarily led to a better measurement of the object's VHE flux and its photon spectrum. Combining the improved VHE spectrum with multiwavelength data at lower energies enables robust spectral modeling. The results of the spectral modeling are summarized below.

1. Both leptonic and hadronic scenarios are considered to explain the observed SED, and the hadronic model is clearly preferred. The gamma-ray SED is compatible with cosmic-ray nuclei following a momentum spectrum with index $s \simeq 2.25$. Models with a heavy composition of both cosmic rays and gas were tested and found to be a reasonable match of the data as well, suggesting that gamma-ray-based statements on a possible elemental enrichment of the material in the starburst core are not possible at this time.
2. The observed gamma-ray flux at 100–500 MeV is likely dominated by bremsstrahlung, which implies an electron-to-ion ratio of GeV-scale electrons in M82 that is much larger than that in, e.g., the Milky Way, on account of the near-equality of the energy-loss timescales for pion production and bremsstrahlung.
3. Primary electrons and secondary electrons associated with the protons can explain the observed radio spectrum while not overproducing the diffuse X-ray emission, which is only partly nonthermal. Additional loss processes besides the radiative energy losses of electrons may be at play; otherwise, the GHz-scale radio flux from the secondary electrons would be very close to that from the primary electrons. Advective escape in the galactic wind could be that additional loss process. A significant reduction of the radio flux from the secondary electrons by, e.g., a higher gas density than assumed here is not possible, because the implied bremsstrahlung flux at a few hundred MHz would exceed the observed level.
4. The lifetime of cosmic rays in M82 is much shorter than the duration of the starburst, suggesting calorimetric behavior. If a significant loss channel for electrons is nonradiative, for example, by escape, then the radiation output is only partially calorimetric and probably likewise for cosmic-ray nuclei.
5. The soft spectral index of $s \simeq 2.25$ for the cosmic-ray source spectrum that the spectral modeling seems to prefer is in line with results for individual supernova remnants. Among the possible reasons for spectra softer than the test-particle limit of diffusive shock acceleration are inefficient turbulence driving upstream of aged shocks, the high temperature of previously shocked upstream plasma, or the small speed of shocks transmitted into filaments of dense gas in the starburst core.

Acknowledgments

This research is supported by grants from the U.S. Department of Energy Office of Science, the U.S. National Science Foundation, and the Smithsonian Institution; by NSERC in Canada; and by the Helmholtz Association in Germany. This research used resources provided by the Open Science Grid, which is supported by the National Science Foundation and the U.S. Department of Energy's Office of Science, and resources of the National Energy Research Scientific Computing Center (NERSC), a U.S. Department of Energy Office of Science User Facility operated under contract No. DE-AC0205CH11231. We acknowledge the excellent work of the technical support staff at the Fred Lawrence Whipple Observatory and at the collaborating institutions in the construction and operation of the instrument.

ORCID iDs

A. Acharyya https://orcid.org/0000-0002-2028-9230
C. B. Adams https://orcid.org/0000-0002-9021-6192
P. Bangale https://orcid.org/0000-0002-3886-3739
J. T. Bartkoske https://orcid.org/0000-0002-9675-7328
W. Benbow https://orcid.org/0000-0003-2098-170X
J. H. Buckley https://orcid.org/0000-0001-6391-9661
A. Duerr https://orcid.org/0000-0003-1716-4119
M. Errando https://orcid.org/0000-0002-1853-863X
A. Falcone https://orcid.org/0000-0002-5068-7344
Q. Feng https://orcid.org/0000-0001-6674-4238
J. Foote https://orcid.org/0000-0002-2944-6060
L. Fortson https://orcid.org/0000-0002-1067-8558
A. Furniss https://orcid.org/0000-0003-1614-1273
W. Hanlon https://orcid.org/0000-0002-0109-4737
D. Hanna https://orcid.org/0000-0002-8513-5603
O. Hervet https://orcid.org/0000-0003-3878-1677
C. E. Hinrichs https://orcid.org/0000-0001-6951-2299
J. Holder https://orcid.org/0000-0002-6833-0474
T. B. Humensky https://orcid.org/0000-0002-1432-7771

W. Jin https://orcid.org/0000-0002-1089-1754
M. N. Johnson https://orcid.org/0009-0008-2688-0815
P. Kaaret https://orcid.org/0000-0002-3638-0637
D. Kieda https://orcid.org/0000-0003-4785-0101
T. K. Kleiner https://orcid.org/0000-0002-4260-9186
N. Korzoun https://orcid.org/0000-0002-4289-7106
S. Kumar https://orcid.org/0000-0002-5167-1221
M. J. Lang https://orcid.org/0000-0003-4641-4201
M. Lundy https://orcid.org/0000-0003-3802-1619
G. Maier https://orcid.org/0000-0001-9868-4700
M. J. Millard https://orcid.org/0000-0001-7106-8502
C. L. Mooney https://orcid.org/0000-0001-5937-446X
P. Moriarty https://orcid.org/0000-0002-1499-2667
R. Mukherjee https://orcid.org/0000-0002-3223-0754
W. Ning https://orcid.org/0000-0002-6121-3443
S. O'Brien https://orcid.org/0000-0002-9296-2981
R. A. Ong https://orcid.org/0000-0002-4837-5253
M. Pohl https://orcid.org/0000-0001-7861-1707
E. Pueschel https://orcid.org/0000-0002-0529-1973
J. Quinn https://orcid.org/0000-0002-4855-2694
K. Ragan https://orcid.org/0000-0002-5351-3323
D. Ribeiro https://orcid.org/0000-0002-7523-7366
I. Sadeh https://orcid.org/0000-0003-1387-8915
L. Saha https://orcid.org/0000-0002-3171-5039
M. Santander https://orcid.org/0000-0001-7297-8217
R. Shang https://orcid.org/0000-0002-9856-989X
M. Splettstoesser https://orcid.org/0000-0003-3407-9936
D. Tak https://orcid.org/0000-0002-9852-2469
D. A. Williams https://orcid.org/0000-0003-2740-9714
S. L. Wong https://orcid.org/0000-0002-2730-2733
J. Woo https://orcid.org/0009-0001-6471-1405

References

Abdo, A. A., Ackermann, M., Ajello, M., et al. 2009, ApJS, 183, 46
Abdo, A. A., Ackermann, M., Ajello, M., et al. 2010, A&A, 512, A7
Abeysekara, A. U., Archer, A., Benbow, W., et al. 2020, ApJ, 894, 51
Acero, F., Aharonian, F., Akhperjanian, A. G., et al. 2009, Sci, 326, 1080
Adams, C. B., Benbow, W., Brill, A., et al. 2022, A&A, 658, A83
Adebahr, B., Krause, M., Klein, U., et al. 2013, A&A, 555, A23
Aharonian, F., Ait Benkhali, F., Aschersleben, J., et al. 2024, A&A, 686, A308
Ajello, M., Di Mauro, M., Paliya, V. S., & Garrappa, S. 2020, ApJ, 894, 88
Bachetti, M., Harrison, F. A., Walton, D. J., et al. 2014, Natur, 514, 202
Badmaev, D. V., Bykov, A. M., & Kalyashova, M. E. 2022, MNRAS, 517, 2818
Basu, A., Mitra, D., Wadadekar, Y., & Ishwara-Chandra, C. H. 2012, MNRAS, 419, 1136
Berge, D., Funk, S., & Hinton, J. 2007, A&A, 466, 1219
Bhatt, M., Sushch, I., Pohl, M., et al. 2020, APh, 123, 102490
Blom, J. J., Paglione, T. A. D., & Carramiñana, A. 1999, ApJ, 516, 744
Blumenthal, G. R., & Gould, R. J. 1970, RvMP, 42, 237
Brightman, M., Walton, D. J., Xu, Y., et al. 2020, ApJ, 889, 71
Brose, R., Pohl, M., Sushch, I., Petruk, O., & Kuzyo, T. 2020, A&A, 634, A59
Butt, Y. 2009, Natur, 460, 701
Caprioli, D., Haggerty, C. C., & Blasi, P. 2020, ApJ, 905, 2
Carlstrom, J. E., & Kronberg, P. P. 1991, ApJ, 366, 422
Celli, S., Morlino, G., Gabici, S., & Aharonian, F. A. 2019, MNRAS, 490, 4317
Cho, J., Vishniac, E. T., Beresnyak, A., Lazarian, A., & Ryu, D. 2009, ApJ, 693, 1449
Christiansen, J. 2017, ICRC (Busan), 301, 789
Christiansen, J. 2018, VERITAS Memos
Cogan, P. 2008, ICRC (Mérida), 3, 1385
Condon, J. J. 1992, ARA&A, 30, 575
Das, S., Brose, R., Meyer, D. M. A., et al. 2022, A&A, 661, A128
de Cea del Pozo, E., Torres, D. F., & Marrero, A. Y. R. 2009, ApJ, 698, 1054
Dessart, L., John Hillier, D., & Audit, E. 2017, A&A, 605, A83
Ellison, D. C., Drury, L. O., & Meyer, J.-P. 1997, ApJ, 487, 197
Fenech, D. M., Muxlow, T. W. B., Beswick, R. J., Pedlar, A., & Argo, M. K. 2008, MNRAS, 391, 1384
Fomin, V. P., Stepanian, A. A., Lamb, R. C., et al. 1994, APh, 2, 137
Förster Schreiber, N. M., Genzel, R., Lutz, D., & Sternberg, A. 2003, ApJ, 599, 193
Fossey, S. J., Cooke, B., Pollack, G., Wilde, M., & Wright, T. 2014, CBET, 3792, 1
Ginzburg, V. L., & Syrovatskii, S. I. 1964, The Origin of Cosmic Rays (Oxford: Pergamon)
Goobar, A., Johansson, J., Amanullah, R., et al. 2014, ApJL, 784, L12
Götting, N. 2006, PhD thesis, Universität Hamburg
H. E. S. S. Collaboration 2020, NatAs, 4, 167
Huang, C. Y., Park, S. E., Pohl, M., & Daniels, C. D. 2007, APh, 27, 429
Huang, C. Y., & Pohl, M. 2008, APh, 29, 282
Hughes, D. H., Gear, W. K., & Robson, E. I. 1994, MNRAS, 270, 641
Jackson, N., Battye, R. A., Browne, I. W. A., et al. 2007, MNRAS, 376, 371
Kardashev, N. S. 1962, SvA, 6, 317
Kieda, D. B. 2011, ICRC (Beijing), 9, 14
Klein, U., Wielebinski, R., & Morsi, H. W. 1988, A&A, 190, 41
Knapen, J. H., Erroz-Ferrer, S., Roa, J., et al. 2014, A&A, 569, A91
Konstantopoulos, I. S., Bastian, N., Smith, L. J., et al. 2009, ApJ, 701, 1015
Kronberg, P. P., Biermann, P., & Schwab, F. R. 1985, ApJ, 291, 693
Lacki, B. C., & Thompson, T. A. 2012, ApJ, 762, 29
Lerche, I., & Schlickeiser, R. 1982, MNRAS, 201, 1041
Li, T.-P., & Ma, Y.-Q. 1983, ApJ, 272, 317
Maier, G., & Holder, J. 2017, ICRC (Busan), 301, 747
Matsumoto, H., Tsuru, T. G., Koyama, K., et al. 2001, ApJL, 547, L25
Melioli, C., de Gouveia Dal Pino, E. M., & Geraissate, F. G. 2013, MNRAS, 430, 3235
Melo, V. P., Muñoz-Tuñón, C., Maìz-Apellániz, J., & Tenorio-Tagle, G. 2005, ApJ, 619, 270
Meyer, D. M. A., Petrov, M., & Pohl, M. 2020, MNRAS, 493, 3548
Meyer, J.-P., Drury, L. O., & Ellison, D. C. 1997, ApJ, 487, 182
Nagai, T. 2005, PhD thesis, Univ. Utah
Naylor, B. J., Bradford, C. M., Aguirre, J. E., et al. 2010, ApJ, 722, 668
Otte, A. N., Gebremedhin, L., Kaplan, K., & Long, D. 2011, ICRC (Beijing), 9, 247
Paglione, T. A. D., & Abrahams, R. D. 2012, ApJ, 755, 106
Park, N. & VERITAS Collaboration 2015, ICRC (The Hague), 34, 771
Persic, M., Rephaeli, Y., & Arieli, Y. 2008, A&A, 486, 143
Pohl, M. 1993, A&A, 270, 91
Pohl, M. 1994, A&A, 287, 453
Pohl, M. 2021, ApJ, 921, 121
Rieke, G. H., Lebofsky, M. J., Thompson, R. I., Low, F. J., & Tokunaga, A. T. 1980, ApJ, 238, 24
Rohlfs, K., & Wilson, T. L. 2004, Tools of Radio Astronomy (Berlin: Spinger),
Sakai, S., & Madore, B. F. 1999, ApJ, 526, 599
Sander, A., Hamann, W. R., & Todt, H. 2012, A&A, 540, A144
Sander, A. A. C., Hamann, W. R., Todt, H., et al. 2019, A&A, 621, A92
Schekochihin, A. A., & Cowley, S. C. 2007, in Magnetohydrodynamics: Historical Evolution and Trends, ed. S. Molokov, R. Moreau, & H. K. Moffatt (Berlin: Springer), 85
Smith, P. A., Brand, P. W. J. L., Mountain, C. M., Puxley, P. J., & Nakai, N. 1991, MNRAS, 252, 6P
Todt, H., Sander, A., Hainich, R., et al. 2015, A&A, 579, A75
Ustamujic, S., Orlando, S., Greco, E., et al. 2021, A&A, 649, A14
VERITAS Collaboration, Acciari, V. A., Aliu, E., et al. 2009, Natur, 462, 770
Voelk, H. J. 1989, A&A, 218, 67
Völk, H. J., Aharonian, F. A., & Breitschwerdt, D. 1996a, SSRv, 75, 279
Weiß, A., Neininger, N., Hüttemeister, S., & Klein, U. 2001, A&A, 365, 571
Westmoquette, M. S., Gallagher, J. S., Smith, L. J., et al. 2009, ApJ, 706, 1571
Williams, P. K. G., & Bower, G. C. 2010, ApJ, 710, 1462
Yoast-Hull, T. M., Everett, J. E., Gallagher, J. S. I., & Zweibel, E. G. 2013, ApJ, 768, 53